1 **Process water recirculation for catalytic hydrothermal carbonization of anaerobic**

2 **digestate: Water-Energy-Nutrient Nexus**

3

4 Mingjing He [a], Yang Cao [a], Zibo Xu [a], Siming You [b], Roger Ruan [c], Bin Gao [d], Ka-Hing Wong

5 [e, f], Daniel C.W. Tsang [a, f*]

6

7 [a] Department of Civil and Environmental Engineering, The Hong Kong Polytechnic

8 University, Hung Hom, Kowloon, Hong Kong, China

9 [b] University of Glasgow, James Watt School of Engineering, Glasgow G12 8QQ, UK

10 [c] Department of Bioproducts and Biosystems Engineering, University of Minnesota, 1390

11 Eckles Ave., St. Paul, MN 55108, USA

12 [d] Department of Agricultural and Biological Engineering, University of Florida, Gainesville
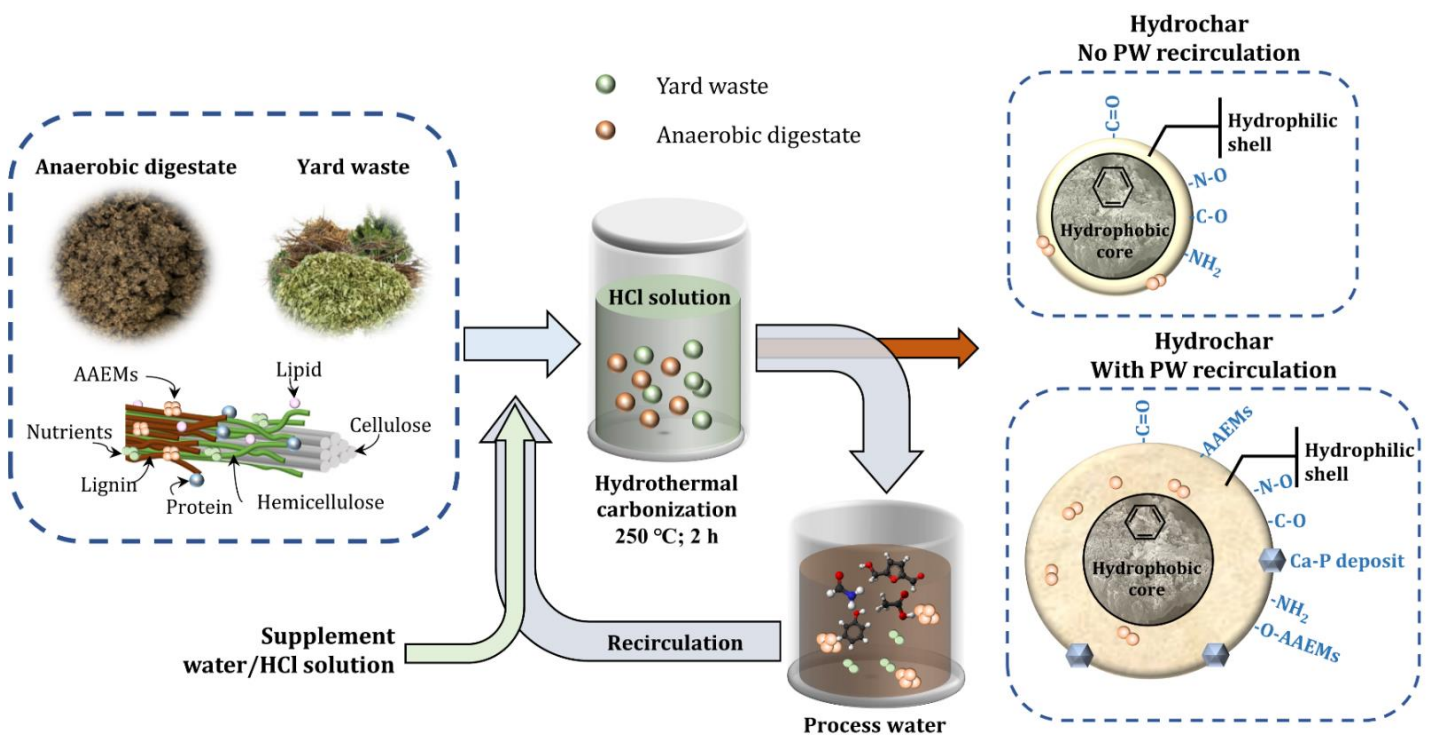
13 FL, 32611, USA

14 [e] Department of Applied Biology and Chemical Technology, The Hong Kong Polytechnic

15 University, Hong Kong, China

16 [f] Research Institute for Future Food, The Hong Kong Polytechnic University, Hung Hom,

17 Kowloon, Hong Kong, China

18

19 * Corresponding author: **dan.tsang@polyu.edu.hk**

20 **Graphical Abstract**

Abstract

The process water (PW) from acid-catalyzed hydrothermal carbonization (HTC) is still an environmental burden due to the enriched organics, nutrients, and salts. This study proposed a novel strategy to valorize food waste digestate into multifunctional hydrochar by recirculating the PW in the HCl-catalyzed HTC process. The produced multifunctional hydrochar could be utilized as a high-quality solid fuel with HHV of 27.9 MJ kg^{-1} (hydrochar without PW recirculation) and a slow-release fertilizer by converting the complex Ca and P compounds from the food waste digestate into a Ca-P deposit (hydroxyapatite) with more than a 93% P recovery rate (hydrochar with PW recirculation). Adding fresh HCl in the HTC PW recirculation system only displayed a marginal catalytic impact on the hydrochar properties after two cycles of recirculation. This study demonstrated the importance of inherent Ca in the feedstocks and the dual role of HCl in the HTC with PW recirculation.

1 Introduction

Anaerobic digestion (AD) process is a widely adopted technology to generate renewable energy (biogas) from wet organic waste, which assists us to offset the adverse environmental impacts of waste disposal and to achieve carbon neutrality (Hao et al., 2019). However, the resultant AD residues (referred to as digestate) contain a high moisture content (> 70%) with semi-stabilized carbon, nutrients, microbial cells, and inorganic minerals (*e.g.,* salts and metals) (Dutta et al., 2021). However, the direct application of digestate or digestate-derived compost as a soil amendment still faces prevalent limitations including phytotoxic concerns, high greenhouse gas emissions, nutrient leaching and water pollution, pathogen exposure, strict implementation requirements, and low market competitiveness (Monlau et al., 2015). Hence, hydrothermal carbonization (HTC) process without an energy-intensive pre-drying process has recently emerged as a feasible strategy for efficient digestate utilization as value-added hydrochar (Cao et al., 2021).

It is noted that the high ash content of the digestate (> 30 wt.%) has limited its energy conversion and utilization in practical applications. Our latest study developed a novel technology that applies acid-catalyzed co-HTC of digestate with lignocellulosic biomass (*i.e.,* fallen leaves) to decrease the ash content in the prepared hydrochar with improving carbon recovery and energy potential (He et al., 2021b). Nevertheless, the acid-catalytic HTC process may cause the enrichment of the various reaction products, intermediates, and secondary polymeric compounds with high organic and nutrient contents in the generated aqueous phase

4

57   (process water, PW). The costs of wastewater treatment and disposal could account for up to

58   90% of the waste treatment for the hydrothermal process (Usman et al., 2019). Moreover, the

59   direct disposal of valuable nutrient elements contradicts the circular economy related to the

60   green chemistry. According to the latest report from McKinsey&Company (2021),

61   recirculating the generated wastewater is a practical strategy to reduce the water footprints and

62   lower the overall carbon emissions toward a sustainable Energy-Water-Carbon nexus.

63   Recent studies have revealed that recirculating PW for the HTC process could increase the

64   yield of hydrochar with an improved energy recovery (**Table 1**). This could be attributed to the

65   promoted acidolysis and condensation reactions by the acidic intermediates (*e.g.,* volatile fatty

66   acids) that accumulated in the PW (Leng et al., 2020; Wang et al., 2019), especially for the

67   lignocellulosic feedstocks (Leng et al., 2020; Usman et al., 2019). Nevertheless, for the ash-

68   rich feedstocks such as sewage sludge (**Table 1**), although PW recirculation of HTC process

69   was found effective to increase the energy recovery efficiency by 4−15%, the energy properties

70   of hydrochar could hardly meet the requirements of high-quality fuel (Xu et al., 2020). The

71   major added values of PW recirculation appear to be limited to the mitigation of wastewater

72   discharge.

73   In contrast to sewage sludge, the PW from the HTC of food waste digestate (FWD)

74   normally contains a high alkalinity, owing to the release of inherent alkali and alkaline earth

75   metals (AAEMs) from the feedstock (Dutta et al., 2021; He et al., 2022). The released AAEMs

76   (*e.g.,* Ca) can facilitate the biomass conversion (*e.g.,* deoxygenation and ketonization reaction),

77   govern the solid-liquid distribution of products and the evolution of hydrochar structure (Gupta

78   et al., 2021). This may affect the transformation of hydrochar and nutrients (N and P) as an *in-*

79   *situ* catalyst in the HTC process. Moreover, the protein-rich nature of FWD may result in the

80   formation of protein-derived intermediates (*e.g.,* Maillard reaction products (He et al., 2021b;

81   Xu et al., 2020)), which is different from that of lignocellulosic feedstocks, especially when

82   considering its fate during the catalytic HTC process. Therefore, the co-accumulation of

83   AAEMs, organic acids, and N-containing compounds, could present a unique composition of

84   PW for its recirculation in the HTC process of FWD, while the changes of solid-liquid

85   distribution and products characteristics remain unknown.

86   Given the considerable inherent P content from the microbial cells and extracellular

87   polymeric substances (EPS) in the digestate (Huang et al., 2015), the acid-catalyzed HTC

88   process may also achieve effective extraction and transformation of P from the complex solid

89   form to the soluble liquid phase. Nutrient recovery from the under-utilized PW is a research

90   hotspot for fostering a circular economy. Current technologies generally require chemical

91   addition, integration of biological processes, and/or membrane separation to realize P recovery

92   (Aragón-Briceño et al., 2021). For instance, CaO (5−50%) was adopted in the thermochemical

93   process to facilitate the transformation of P in sludge into hydroxyapatite ($Ca_5(PO_4)_3(OH)$; pK_{sp}

94   = 58.5) as a pH-sensitive and slow-release fertilizer (Shi et al., 2019; Zheng et al., 2020).

95   Nevertheless, previous studies did not consider the potential co-effect of accumulated HTC

96   intermediates and AAEMs during the PW recirculation on the nutrient transformation

97   behaviour in the HTC system. To enhance simultaneous energy and nutrient recovery in the

98   FWD valorization, fundamental knowledge about the evolution of product distribution and

99   properties is necessary to better design HTC PW recirculation.

100   By comparing different PW recirculation scenarios with various dosage frequency of fresh

101   catalysts, this study aims to: (i) clarify the dual role of HCl in determining the hydrochar energy

102   properties, nutrient transformation, and PW composition; (ii) reveal the co-effect of the

103   accumulation of inherent AAEMs, reaction intermediates, and residual acid catalyst on the

104   solid-liquid transformation of carbon and nutrients (N and P) in the HTC system; and (iii)

105   identify cost-effective HTC PW recirculation conditions for producing multifunctional FWD

106   hydrochar with a minimized water footprint. To close the resource loop and boost the Water-

107   Energy-Nutrient Nexus, this study provides new insights into the valorization of anaerobic

108   digestate by recirculating HCl-catalyzed HTC PW to produce multifunctional hydrochar as a

109   high-quality solid fuel and a slow-release fertilizer.

2   Materials and methods

2.1   Materials

112   The applied biomass feedstocks were locally sourced digestate from an AD process of food

113   waste (FWD, collected from the Hong Kong O●PARK1 that handles up to 200 tonnes of food

114   waste per day) and wet yard waste (YW, a mixture of grass clippings, fallen leaves, and small

115   branches, collected from the Hong Kong Environmental Protection Department). The collected

116   biomass was oven-dried at 105 °C until it reached a constant weight. The dried FWD and YW

117   were crushed to pass an 18-mesh screen and sealed for further processing. The properties of

118   the feedstocks (**Table 2**) were characterized according to **Section 2.3.1**. All the chemicals

119   applied in this study were of analytical grade.

2.2   Hydrothermal carbonization process

121   Based on our recent study (He et al., 2021b), 0.5 M HCl catalytic co-HTC of FWD and

122   YW with a mass ratio of 1:1 exhibited superior performance in terms of energy recovery and

123   carbon utilization efficiency. In this context, the same HTC conditions were adopted in this

124   work as baseline experiments (first cycle; R1). Specifically, 35 g of feedstocks (17.5 g FWD

125   and 17.5 g YW) were mixed with 350 mL of 0.5 M HCl solution. The HTC experiments were

126   conducted in a 500-mL Parr 4575A reactor. The reactor was heated to 250 ± 5 ℃ with a

127   residence time of 2 h and a stirring speed of 300 ± 2 rpm. The reaction was sequenced by

128   cooling with water to room temperature. The HTC slurry was filtered through a vacuum filter

129   (0.45-μm); the separated solid (hydrochar) was oven-dried at 60 ℃ for 24 h and weighed for

130   the yield calculation (yield = $m_{hydrochar}/m_{feedstock}$), then sealed for further analysis. The separated

131   PW was stored at 4 ℃ in the dark for subsequent analysis and recirculation experiments.

132   In the PW recirculation tests, the solid-to-liquid ratio of 1:10 (35 g feedstock in 350 mL

133   solution) was the same as the baseline experiments (R1). Given the water retained in the

134   hydrochar and the water required for analysis, 80% (280 mL) of PW was recirculated and

135   supplemented with 20% (70 mL) of fresh solution (deionized (DI) water or HCl solution). Two

136   scenarios with PW recycling up to five times (i.e., six cycles in total for each scenario) were

137   designed to compare the catalytic ability of recycled catalyst, which are (1) Pulse (P) scenario:

138   only added HCl at the 4th cycle (R4) to obtain 0.5 M HCl in the overall system (calculated

139   based on mass balance) and DI water for other cycles; the samples obtained for each cycle were

140   designated as "P_number of cycle" (*e.g.,* P_R1); and (2) Continuous (C) scenario: adding HCl

141   every cycle to obtain 0.5 M HCl in the overall system (calculated based on mass balance), the

142   samples obtained were named as "C_number of cycle" (*e.g.,* C_R1).

143   **2.3   Analytical methods**

144   **2.3.1   Characterization of hydrochar samples**

145   The proximate composition (volatile matter (VM), ash content, and fixed carbon (FC,

146   calculated by difference); wt.% on a dry basis) was determined by ASTM D1762-84 Standard

147   Method. The elemental analysis (C, H, N, and S; wt.% on a dry basis) was carried out using an

148   elemental analyzer (EA, Vario EL cube, Germany), the O content (wt.%) was calculated by

149   difference ([O] = 100-[C]-[H]-[N]-[S]-ash). **Eq.1−3** were applied to calculate the fuel ratio

150   (FR), higher heating value (HHV), and energy recovery efficiency of the hydrochar,

151   respectively (He et al., 2021a). The carbon retention rate in the hydrochar was calculated based

152   on the carbon balance by **Eq.4**.

153                 $$\text{FR} \left(/ \right) = \frac{FC}{VM} \qquad \qquad \textbf{Eq.1}$$

154                 $$\text{HHV} \left(\text{MJ kg}^{-1} \right) = 0.3517C + 1.1626H + 0.1047S - 0.111O \qquad \textbf{Eq.2}$$

155                 $$\text{Energy recovery} \left(/ \right) = \frac{\text{yield} \times \text{HHV}_{\text{hydrochar}}}{\text{HHV}_{\text{feedstock}}} \qquad \textbf{Eq.3}$$

156                 $$\text{C retention}_{\text{hydrochar}} = \frac{[C]_{\text{hydrochar}} \times m_{\text{hydrochar}}/100}{([C]_{\text{feedstock}} \times \frac{m_{\text{feedstock}}}{100}) + (TOC_{PW} \times V_{PW} \times 0.8)} \qquad \textbf{Eq.4}$$

157   where V_{PW} is the volume of PW (0.35 L); $m_{\text{hydrochar}}$ is the mass of hydrochar (g);

158      $m_{\text{feedstock}}$ is the mass of feedstock (g); TOC_{PW} is the total organic carbon (TOC)

159   concentration of process water (g L^{-1}); and 0.8 is the PW recirculation rate that 80% of PW

160   was recirculated with 20% of DI water/HCl solution supplemented.

161   The AAEMs contents *(i.e., K, Na, Ca, and Mg)* in the hydrochar were determined by

162   USEPA Method 3050B; the hydrochar was digested by concentrated HNO_3/H_2O_2. The digested

163   residues were dissolved by 5% HNO_3 and then filtered (0.45-μm) for the inductively coupled

164   plasma   optical   emission   spectroscopy   (ICP-OES,   Spectro)   measurement.   A

165   Thermogravimetric Analyzer-Differential Scanning Calorimeter (TG-DSC; PerkinElmer

166   Pyris1) in an airflow environment was applied to evaluate the combustion behaviour of the

167   hydrochar. The associated experimental settings and the calculation details for combustion

168   characterization were same as our previous study (He et al., 2021b).

169   X-ray photoelectron spectroscopy (XPS, Thermo Scientific Nexsa) with Al Kα radiation

170   was applied to reveal the surface composition and chemical states of the hydrochar. C1s at

171   284.8 eV was used for the binding energy calibration of characteristic peaks. The morphology

172   of the hydrochar samples was evaluated by the scanning electron microscopy with energy

173   dispersive spectroscopy analysis (SEM-EDX, JEOL 6490, Japan). Fourier transform infrared

174   spectroscopy (FT-IR) was used to investigate the evolution of surface functional groups. The

175   SMT (Standard Measurement and Test) sequential extraction method was applied to evaluate

176   the P species in the hydrochar (Ruban et al., 1999); and the concentration of total phosphate

177   (PO_4^{3-}) in the extraction supernatant was measured by PhosVer 3 Method with a colorimeter

178   (HACH).

179   **2.3.2   Analysis of process water**

180   To determine the contents of AAEMs in the PW and water-soluble AAEMs of hydrochar

181   (solid-to-liquid ratio = 1:200), the filtered (0.45-μm) liquid samples were digested by

182   concentrated HNO_3 then dissolved by 5% HNO_3 to determine the AAEMs concentrations by

183   ICP-OES. The AAEMs balance and distribution in the HTC system were calculated by **Eq.5**

184   and **Eq.6**.

185          $$\text{AAEMs in PW (\%)} = \frac{[\text{AAEMs}]_{PW} \times V_{PW}}{[\text{AAEMs}]_{PW} \times V_{PW} + [\text{AAEMs}]_{hydrochar} \times m_{hydrochar}} \times 100 \qquad \textbf{Eq.5}$$

186          $$\text{AAEMs in hydrochar (\%)} = 1 - \text{AAEMs in PW (\%)} \qquad \textbf{Eq.6}$$

187   where $[\text{AAEMs}]_{PW}$ is the sum of Na, K, Ca, and Mg concentration (g L^{-1}) in PW and

188    $[\text{AAEMs}]_{hydrochar}$ is the sum of Na, K, Ca, and Mg concentration (mg g^{-1}) in the hydrochar.

189   Three-dimensional excitation-emission matrix (3D-EEM) fluorescence spectroscopy (FS5

190   Spectrofluorometer) with parallel factor (PARAFAC) modelling analysis (MATLAB R2020a

191   with DOMFlour toolbox) was applied to identify and quantify the organic matter evolution

192   during the recirculation of HTC PW. Fluorescence 3D-EEM was scanned at

193   excitation/emission wavelengths of 200-450/300-550 nm with 5-nm interval. All the process

194   water samples were diluted 200 times by DI water to avoid inner filter effects. The samples

195   3D-EEM was Raman calibrated and had a DI water blank value scanned on the same day

196   subtracted. All the samples (12 samples in total) were measured at least 5 times (64 groups of

197   data in total including blank samples) to ensure enough sample size for the PARAFAC analysis

198   with split-half validation. The MATLAB code applied for PARAFAC analysis was adapted

199   from the tutorial given by Stedmon and Bro (2008).

200   The total organic carbon (TOC) and total nitrogen (TN) were analyzed by a TOC-L/TN

201   analyzer (Shimadzu Corporation). A gas chromatography-mass spectrometry (Agilent 5977B

202   GC/MSD; HP-5MS column) coupled with the NIST database was used to identify the

203   significant compounds for selected dichloromethane extracted PW samples. A UV-vis

204   spectrophotometer (200−800 nm; 0.5 nm interval) was used to measure the UV-vis absorbance

205   value and reveal the aromaticity of the PW by SUVA$_{254}$ (**Eq.7**).

206
$$SUVA_{254} = \frac{2.303A_{254}}{I_L \times TOC} \qquad\qquad \textbf{Eq.7}$$

207   where A_{254} is the absorbance at 254 nm, I_L is the path length of the optical cell in meters (l

208   = 0.01 m), and TOC is the total organic carbon content in the PW.

209   3   Results and discussion

210   3.1   AAEMs accumulation by process water recirculation

211   The acid-catalyzed HTC process facilitated the transformation of AAEMs from solid

212   feedstocks (~65 mg g^{-1}) into the liquid phase due to proton-promoted dissolution by HCl. Only

213   14% of AAEMs were retained in the hydrochar after the first cycle of the HTC process (P_R1

214   and C_R1, **Figure 1a**). Calcium was the primary AAEMs in both R1 hydrochar (65.6 ± 0.3%)

215   and PW (88.6 ± 0.1%), attributed to the rich content of inherent Ca (90.1 ± 0.2%) from the

216   FWD (*e.g.,* undigested bones).

217   By recirculating the PW, AAEMs in the hydrochar significantly increased from 17.6 to

218   71.4−74.3 mg g^{-1} from R1 to R2, and no identifiable trend of AAEMs accumulation in the

219   hydrochar was found after R2 owing to the equilibrium deposition (**Figure 1c**) and possible

220   pH buffer by the accumulated organic acid intermediates (see **Section 3.2**). In addition, a linear

221   rise of the total AAEMs concentrations in the PW was observed (**Figure 1b**). The accumulation

222 rate of scenario C (slope = 0.28; R^2 = 0.97) was slightly higher than scenario P (slope = 0.24;

223 R^2 = 0.99), as more AAEMs were dissolved in the PW of scenario C due to the lower pH by

224 replenishment of HCl each cycle. A noticeable increase in AAEMs distribution was found in

225 the hydrochar after the first recirculation (46%, P_R2 and C_R2, **Figure 1a**), which then

226 decreased to 25−31% after R2 with the increase of distribution in PW. The solid-liquid

227 distribution of AAEMs was significantly affected by the pH of the PW, and the increased cycles

228 of recirculation (R3 to R6) and addition of fresh HCl facilitated the transformation of AAEMs

229 to the liquid phase (**Figure 1c**).

230   R2 hydrochar exhibited the highest AAEMs distribution (46%), probably due to the acidic

231 catalyst consumption and AAEMs accumulation in the PW, which was in line with the pH

232 results. It is noted that Ca (11.6 mg g^{-1} for P/C_R1, 6.1-fold increase for P_R2, and 4.9-fold

233 increase for C_R2) exhibited the highest accumulation in the hydrochar and Mg (0.9 mg g^{-1} for

234 P/C_R1; ~1.7-fold increase for P_R2 and C_R2) showed a moderate accumulation. In contrast,

235 the concentrations of K (0.9−1.2 mg g^{-1}) and Na (4.3−4.6 mg g^{-1}) in the hydrochar were not

236 affected by the PW recirculation. The different valences of the AAEMs contributed to the

237 different accumulation extents in the hydrochar, as the bonding stability of divalent Ca and Mg

238 is stronger than that of monovalent alkali metals (K and Na) (Feng et al., 2018).

239   The extraction ratio of water-soluble AAEMs of R1 hydrochar was 0.71±0.10, indicating

240 the high solubility of AAEMs with the limited precipitate formation in the hydrochar obtained

241 from the initial catalytic HTC process (**Figure 1d**). By recirculating the PW with enriched

242 intermediates and residual AAEMs, the average extraction ratio was 3.3−4.7-fold lower for the

243 hydrochar from scenario P and 1.9−2.6-fold lower for the hydrochar from scenario C, implying

244 the formation of Ca and Mg species with low water solubilities (*e.g.,* oxalates and apatite-P)

245 with recycled intermediates (Liu et al., 2021b; Shi et al., 2021). As shown in **Figure 1d**, PW

246 recirculation with scenario P had little impact on the concentrations of water-soluble AAEMs

247 (11.1−14.8 mg g^{-1}), with a slight increase observed at P_R4 (from 0.15 of P_R2 to 0.22 of

248 P_R4) due to the addition of fresh HCl. In scenario C, the highest concentration of water-

249 soluble AAEMs (23.7 mg g^{-1}) with less AAEMs precipitation was found for C_R2 because of

250 the newly added HCl and the residual acid from the first cycle (R1) that more AAEMs were

251 dissolved (*e.g.,* $CaCl_2$). This observation was validated by the DTG curves (see supplementary

252 materials) that a small peak at 550−750 ℃ for Ca deposits (He et al., 2021b) was only found

253 for the hydrochar samples from scenario P. In a nutshell, by supplementing fresh HCl in each

254 cycle (scenario C), the form of AAEMs was more water-soluble with a lower content (4−6%

255 lower) of AAEMs in the hydrochar.

256 **3.2 Intermediates in process water**

257 Given the complex HTC reaction pathway (see supplementary materials), intermediates

258 with higher hydrophilicity (*e.g.,* organic acids) will take part in the formation of hydrophilic

259 shell on the hydrochar by PW recirculation, while intermediates with higher aromaticity (*e.g.,*

260 furfural) and undegraded lignin would form aromatic core structure by repolymerization (Leng

261 et al., 2020). Understanding the characteristics of intermediates in the PW is crucial to reveal

262 the solid-liquid transformation in the HTC process.

263 The TOC content increased stepwise from 10.1 to 21.8−27.8 g L^{-1} after increasing the

264   cycles of PW recirculation from R1 to R6 (2.8-fold for scenario P and 2.1-fold for scenario C)

265   due to the accumulation of soluble organic intermediates (**Figure 2a**). Interestingly, the TOC

266   accumulation behaviour in the PW was affected by the addition of HCl catalyst. A two-stage

267   TOC accumulation was observed for scenario P, and the average TOC accumulation rates for

268   the first stage (P_R1 to P_R3) and second stage (P_R4 to P_R6) were 4.1 and 4.3 g L^{-1} cycle^{-}

269   ^{1}, respectively. While from P_R3 to P_R4, only 1.1 g L^{-1} of TOC was accumulated owing to

270   the supplementation of HCl catalyst at P_R4. Regarding scenario C, the TOC content increased

271   linearly with a 2.4 g L^{-1} cycle^{-1} from 10.2 g L^{-1} for C_R1 to 21.8 g L^{-1} for C_R6, due to

272   continuous replenishment of HCl catalyst to the HTC process. These different results of TOC

273   accumulation could be attributed to the overall higher pH condition of scenario P and the

274   promoted formation of secondary char by an acid catalyst; that is, the dissolved intermediates

275   were repolymerized to an amorphous solid and deposited on the primary char with less organic

276   carbon retained in the PW (Lucian et al., 2018).

277   The SUVA$_{254}$ value of PW ranged between 1.88 and 2.29 L mg^{-1} m^{-1} (**Figure 2a**), revealing

278   that the primary organic intermediates in the PW should be low-molecular-weight organic acids

279   with low aromaticity and low hydrophobicity accumulated through the hydrolysis of

280   carbohydrates (Liu et al., 2021a). Although YW included a high lignin content (30.2%), the

281   extremely recalcitrant nature of lignin restricts its decomposition to dissolvable aromatics

282   (Barta and Ford, 2014). Therefore, lignin was marginally decomposed under a mild

283   thermochemical condition, forming the primary char with an aromatic structure (Cao et al.,

284   2021). The slightly higher SUVA$_{254}$ value of scenario C (2.18 ± 0.07 L mg^{-1} m^{-1}) compared to

285   that of scenario P (2.06 ± 0.14 L mg^{-1} m^{-1}) could be attributed to the repolymerization process

286   facilitated by continuously supplementing the HCl catalyst, such that more organic acids could

287   be converted to intermediates with higher aromaticity (Leng et al., 2020; Lucian et al., 2018).

288   The 3D-EEM spectrum was further determined to evaluate the speciation of intermediates

289   in the HTC PW (**Figure 2b**). Three significant peaks at Peak C ($\lambda_{Ex}/\lambda_{Em}$ = 320–360/420–460

290   nm; humic-like substances), Peak M ($\lambda_{Ex}/\lambda_{Em}$ = 290-310/370-410 nm; marine humic-like

291   substances), and Peak A ($\lambda_{Ex}/\lambda_{Em}$ = 260/400–460 nm; fulvic- and humic-like substances)

292   (Coble et al., 2014) appeared in the PW, suggesting that humic-like substances were the

293   primary compounds. According to the general components information provided by the

294   division of characteristic regions in the EEM maps, the peaks at Region I (tyrosine-like protein),

295   Region II (tryptophan-like protein), and Region IV (soluble microbial by-product-like

296   substances) were insignificant in all PW (**Figure 2b**) (Xiao et al., 2018). This suggested that

297   all the protein-like and microbial-derived substances from FWD were converted to humic-like

298   compounds such as small molecules of heterocyclic amines by Maillard and Mannich reactions

299   (progress of humification transformation) during the HTC process due to the co-existence of

300   protein, carbohydrates, and lignin-derived phenols (Leng et al., 2021; Zhang et al., 2019).

301   Although the peak picking method (**Figure 2b**) could provide a general component

302   division for PW, the PARAFAC analysis was applied to deconvolve the 3D-EEM maps to

303   understand the semi-quantitative evolution of intermediates without the interference of the

304   increasing TOC concentration. Moreover, the deconvolution of EEM maps can better reveal

305   the evolution of the hydrophilic and hydrophobic fractions of PW by the recirculation processes

306   (Xiao et al., 2018). The 3D-EEM maps were normalized by the TOC concentration and three

307   fluorescent components were identified from the 3D-EEM PARAFAC analysis (**Figure 2c**).

308   Component C1 had $\lambda_{Ex}/\lambda_{Em}$ maxima at 335/425 nm, corresponding to the co-occurrence of

309   Peak M and Peak C. A similar peak ($\lambda_{Ex}/\lambda_{Em}$ = 340/426 nm) was also identified by Li et al.

310   (2017) for humic-like substances (*i.e.,* breakdown compounds of lignin) (Carstea et al., 2016;

311   Li et al., 2017). Component C2 (a maximum $\lambda_{Ex}/\lambda_{Em}$ at 355/445 nm) was assigned to the UVA

312   humic-like substances with a larger molecular size and greater aromaticity than C1 (Song et al.,

313   2020). Component C3 exhibited the highest peak at $\lambda_{Ex}/\lambda_{Em}$ of 310/415 nm, covering the peak

314   M, peak A, and peak T (cellular material and their exudates) over $\lambda_{Ex}/\lambda_{Em}$ of 240–320/320–420

315   nm, which could be attributed to the presence of aromatic hydrocarbons in the PW (Carstea et

316   al., 2016; Xiao et al., 2018).

317   By recirculating the PW from R1 to R2, the intensity of C1 increased 8.4-fold for scenario

318   P and 6.0-fold for scenario C, while no remarkable change was found for C2 and C3, suggesting

319   that the accumulated intermediates in PW were dominated by hydrophilic substances (*e.g.,*

320   organic acids) in the first cycle of PW recirculation (Leng et al., 2020; Xiao et al., 2018).

321   Increasing the PW recirculating cycles from R2 to R6 resulted in a decreasing trend of C3 (88.3%

322   decrease for scenario P and 79.2% for scenario C), suggesting that the liquid-to-solid transition

323   and the repolymerization of the hydrochar with the formation of aromatic core structures (Leng

324   et al., 2020; Xu et al., 2020), which was observed as the formation of the hydrochar

325   microspheres by SEM-EDX.

3.3 Evolution of hydrochar properties

3.3.1 Proximate and ultimate properties

The recirculation of PW caused a decrease of FC in both scenario P (9.9−16.4 wt.%) and scenario C (4.6−8.7 wt.%) with an increase of VM (5.0% for P_R6 and 1.6% for C_R6) (**Figure 3a**). The FR (FC/VM) dropped from 0.75 for P_R1/C_R1 to 0.39 for P_R6 and 0.55 for C_R6, indicating a lower potential for energy application. The presence of inherent AAEMs (especially Ca) in the PW can catalyze the hydrolysis of hydrochar by weakening its aromatization and stability (Liu et al., 2021a; Nan et al., 2021), accounting for the lower FC content (see supplementary materials). In addition, AAEMs in the hydrochar would form oxide species such as $Ca(OH)_2$ and $Mg(OH)_2$ with enhanced carbon deposition (Yang et al., 2022). The abundance of organic acid intermediates and AAEMs in the PW tended to form a hydrophilic shell on the hydrochar surface, which can be more volatile during the recirculation steps (as observed by SEM-EDX, see supplementary materials). This lowered the FC and raised the VM content, responsible for a decrease in FR (Leng et al., 2020) and a higher water-soluble organic carbon. Moreover, more OH^- and H^+ radicals may be activated by the AAEMs in the liquid phase, which could accelerate acidic and basic hydrolysis (Yang et al., 2022). Scenario P (average FR = 0.52 ± 0.13) exhibited a lower FR than scenario C (average FR = 0.65 ± 0.07), which might be ascribed to the higher TOC content and lower aromaticity of the PW of scenario P (**Figure 2a**).

The van Krevelen diagram (**Figure 3b**) revealed the evolution of H/C and O/C atomic ratios in the hydrochar during the recirculation of PW. The feedstocks mainly followed the

347 route of decarboxylation and dehydration reactions during the hydrothermal process. The O/C

348 atomic ratio of all the hydrochar was below 0.4, indicating an effective deoxygenation reaction

349 and the increased environmental persistence of the hydrochar with a good carbon sequestration

350 ability (Lehmann et al., 2021). By recirculating the PW, a clear decarboxylation route was

351 observed from P_R1 to P_R2 (in line with the FT-IR results, see supplementary materials).

352 Also, hydrochar from scenario P had higher overall H/C atomic ratios than those of scenario C,

353 suggesting that without supplementing fresh HCl, the short-chain intermediates may form a

354 hydrophilic shell on the hydrochar surface with an increasing H/C atomic ratio and lower

355 aromaticity. Further increasing the cycles of PW recirculation caused no significant change to

356 the hydrochar characteristics in the van Krevelen diagram (**Figure 3b**).

357 **3.3.2 Energy recovery and combustion properties**

358 The yield and energy content (HHV) of the hydrochar reflect the energy recovery

359 efficiency of the HTC process. As shown in **Table 3**, the yield of hydrochar was 0.32−0.33 for

360 P_R1/C_R1, and the recirculation of PW for five times resulted in an average increase in yield

361 of 10.9% for scenario P and 13.5% for scenario C, respectively. The increasing yield of

362 hydrochar could be attributed to four reasons: (i) inhibition of decomposition reactions by

363 organic acids (Xu et al., 2020); (ii) promoted repolymerization of accumulated intermediates

364 (Leng et al., 2020); (iii) complexation of Ca on the hydrochar surface (Liu et al., 2021b); and

365 (iv) promoted C-C coupling (condensation) by the formed Ca-P deposit (*e.g.,* hydroxyapatite)

366 as weak acid-base catalysts (Sans et al., 2021) (see **Section 3.4**).

367 Given the increasing ash content but decreasing C content of hydrochar (7.3% ash on

368 average for scenario P and 7.2% ash on average for scenario C), the deposition of Ca on the

369 hydrochar surface could be the primary reason for the higher yield. In this context, the highest

370 yield was achieved in the second cycle for P_R2 (0.43) and C_R2 (0.54), probably due to the

371 highest Ca accumulation ratio as discussed in **Section 3.1**. As shown in **Table 3**, the C retention

372 rate in the hydrochar decreased from 0.56 (P_R1) to 0.38 (P_R6) for scenario P. Slightly higher

373 C retention rates for C_R2 (0.62) and C_R3 (0.59) were observed for scenario C, probably

374 owing to the residual acid catalyst that more carbon can be repolymerized into the solid form.

375 The energy content of hydrochar, represented by the HHV value, decreased from 28.0 ± 0.1

376 MJ kg^{-1} in the P_R1/C_R1 hydrochar to 24.9 MJ kg^{-1} in P_R6 and 23.9 MJ kg^{-1} in C_R6 (**Table**

377 **3**) because of the ash accumulation and decrease in FC (see supplementary materials).

378 Nevertheless, an enhancement of the overall energy recovery efficiency was observed, from

379 0.59 for P_R1/C_R1 to 0.68 for scenario P and 0.73 for scenario C, due to the increase in

380 hydrochar yield by recirculating the PW.

381 The combustion behaviour of hydrochar was revealed by the combustion parameters

382 (DTG_m, DTG_{mean}, T_m, T_i, T_b, and the calculated CCI and R_w index; in **Table 3**). P_R1/C_R1

383 exhibited superior combustion properties with the highest CCI index of 11.0 and R_w index of

384 10.2, representing outstanding combustion stability with a comprehensive heat release

385 behaviour. Recirculating the PW led to decreases in the CCI and R_w index (CCI of 4.2−6.9 for

386 scenario P; CCI of 4.1−5.4 for scenario C; R_w of 5.6−7.1 for scenario P; R_w of 5.5−7.1 for

387 scenario C) but an increase of T_i from 202 °C to 211 °C for scenario P and 230 °C for scenario

388 C. The accumulated Ca in the hydrochar after the PW recirculation might form stable bonding

389 with volatile carbon, contributing to the decreased combustion properties with a reduced fire

390 risk during transportation and handling (He et al., 2021b).

391 　　DSC analysis was conducted to evaluate the combustion performance of hydrochar

392 (**Figure 3c-d).** The exothermic DSC peaks between 200−600 ℃ corresponded to the

393 volatilization and combustion of hydrochar. Two peaks at 329 ℃ (low-temperature oxidation

394 zone; LTO zone) and 470 ℃ (high-temperature oxidation zone; HTO zone) were identified for

395 P_R1/C_R1. The exothermic LTO peak mainly involves the oxygenation of light hydrocarbons

396 (*e.g.,* volatile carbon), while the HTO peak corresponds to the oxidation of heavier

397 hydrocarbons or other recalcitrant compounds (Kok and Gundogar, 2013). The peak in the

398 HTO zone (470 ℃) shifted to 515–545 ℃ for P_R3 to P_R6, and 515–530 ℃ for C_R5 to

399 C_R6, suggesting that hydrochar was more resistant to combustion after the PW recirculation,

400 for which the ash accumulation could be the primary reason. In short, although recirculating

401 the PW can augment the energy recovery efficiency, the combustion properties (heat release

402 stability and comprehensive extent of combustion) were negatively affected.

403 **3.3.3　Evolution of carbon and nitrogen species**

404 　　XPS analysis was carried out to evaluate the C and N species distribution in the hydrochar

405 (**Figure 4**). As shown in **Figure 4a**, a decrease of 0.2–2.6% for C-C/C=C and an increase of

406 0.4–4.2% for C-O were observed for the C1a XPS peak ratios, indicating the enrichment of

407 oxygen-containing functional groups on the hydrochar surface by recirculating the PW. This

408 increase was in good agreement with the results of intermediates and proximate analysis that

409 the hydrophilic shell was probably formed on the hydrochar by short-chain organic acids (as

21

410   observed by SEM-EDX, <mark>see supplementary material</mark>). The addition of HCl catalyst was the

411   decisive factor for the evolution of C species on the hydrochar. This resulted in less enrichment

412   of O-containing functional groups during the PW recirculation, probably due to the HCl-

413   catalyzed repolymerization of hydrochar, which was in line with the PW characterization

414   results (**Figure 2**).

415   Regarding the N transformation and solubilization in the HTC system (**Figure 4b**), it was

416   found that recirculating the PW led to both accumulation of soluble N in the liquid phase and

417   enhanced N fixation in the hydrochar, due to the overall higher content of N in the HTC system.

418   The dissolved N (TN) content in the PW increased from 1.5 g L^{-1} to 2.6 g L^{-1} for scenario P

419   and 2.9 g L^{-1} for scenario C. The higher solubilization of N for scenario C was due to the lower

420   initial pH (see supplementary material), because continuously supplementing the HCl catalyst

421   could promote the hydrolysis of organic-N species from the FWD (Aragón-Briceño et al.,

422   2021). Both amino-N (0.70%) and pyridinic-N (0.11%) were identified by XPS N1s analysis

423   for P_R1/C_R1, suggesting the occurrence of Maillard and Mannich reactions in the HTC

424   system (*e.g.,* a nucleophilic attack of an amine on the aldehyde of reducing sugars) (Nicolae et

425   al., 2020). This was in line with the 3D-EEM (**Section 3.2**) and GC-MS results (see

426   supplementary material). By recirculating the PW, the N content in the hydrochar increased

427   from 1.5 wt.% to 2.9 wt.% with the promoted formation of pyridinic-N, pyrrolic-N, and N-

428   oxide surface functional groups, but there was no remarkable change on the atomic ratio of

429   amino-N groups. This could be attributed to the enrichment of protein-derived amino acids in

430   the PW and the formation of heterocyclic-N species, because of crystallization and ring

431   condensation of N-containing intermediates *via* Dies-Alder reaction (Leng et al., 2021). This

432   could slow down the N release rate, if the hydrochar is potentially applied as a soil amendment

433   (Yuan et al., 2018). It was found that scenario P exhibited a higher extent of N fixation in the

434   form of pyridinic-N, while the formation of N-oxide and pyrrolic-N were observed for scenario

435   C, due to the facilitated hydrolysis by continuous replenishment of HCl.

3.4   Evolution of phosphorous species

437   During the HTC process, complex P species in the feedstocks (*i.e.,* FWD and YW) can be

438   transformed into the liquid fractions. As shown in **Figure 5**, the high reaction severity of the

439   HCl-catalytic HTC process facilitated the P extraction from the feedstock as well as the

440   breakdown of molecular bonds of P into soluble PO_4^{3-}. The acidity from HCl could catalyze

441   the HTC reactions (*e.g.,* hydrolysis, dehydration, and deamination) and promote the

442   solubilization of inorganic P species. This resulted in P interception in the PW with the highest

443   yield of 3150 ± 14 mg L^{-1} for P_R1/C_R1, with a lower P concentration in the hydrochar

444    $(7.2-7.4$ mg $g^{-1})$. The limited P concentration in the hydrochar was also evidenced by the

445   SEM-EDX mapping, in which the distribution of P on the hydrochar surface was invisible.

446   Although the P_R1/C_R1 contained only a limited amount of P, it possessed the highest

447   water-soluble PO_4^{3-} of 0.52 mg g^{-1} (see supplementary material), owing to the acid dissolution

448   effect.

449   By recirculating the PW, the accumulated Ca could precipitate with the PO_4^{3-} under a

450   relatively high pH condition, resulting in the formation of apatite phosphorus (AP) on the

451   hydrochar (74.7−97.2% of total P), corresponding to the XPS analysis for Ca (see

452 <mark>supplementary material)</mark>. The highest P concentration was found in P_R2/C_R2 (88.0−88.4

453 mg g^{-1}; ~170-fold of P_R1/C_R1) due to the highest P concentration from the PW of R1,

454 while for R3−R6, the remaining P concentrations in the PW from the previous treatment were

455 limited. Accordingly, the PO_4^{3-} concentrations in the recirculated PW decreased to 1.5−231.0

456 mg L^{-1} (13.6−2100-fold decrease) owing to the much higher concentrations of Ca (3.0−6.5 g

457 L^{-1}) in the HTC system (**Figure 1b**), while the water-soluble PO_4^{3-} from the hydrochar mainly

458 depended on the solid-liquid equilibrium controlled by the initial pH condition (<mark>see</mark>

459 <mark>supplementary materials</mark>).

460 **3.5   Cost-benefit analysis and future prospective**

461 A preliminary cost-benefit analysis for a 1000-L scale HTC system is illustrated in **Figure**

462 **6** with the calculation assumptions and unit costs in **Table 4**. To obtain the digestate-derived

463 hydrochar with superior energy properties, the chemical costs of HCl would be the major

464 expenses for the scenario without PW recirculation. Although hydrochar of P_R1/C_R1 had

465 outstanding combustion behaviour and HHV values, the overall energy recovery for the "No

466 PW recirculation" scenario was lower than that of scenario P (20.0% lower) and scenario C

467 (26.6% lower) due to the higher hydrochar yield by PW recirculation. In this context, by

468 recirculating the PW with residual catalyst and accumulated intermediates, scenario P and

469 scenario C can achieve a significant cost saving of 232.9% and 221.9%, respectively, owing to

470 less chemical consumption and higher energy recovery. Although the difference in wastewater

471 treatment costs here was not high in this calculation, the environmental benefits with less

472 discharge of TOC and AAEMs laden wastewater should be considered and valuated.

473   Although recirculating the PW (non-catalytic) augmented the energy recovery efficiency,

474   the produced hydrochar (R2 to R6) might not be suitable for a high-quality solid fuel, due to

475   the high ash content (17.4−24.9%) and low combustion stability. Interestingly, by recirculating

476   the PW of the catalytic HTC process, HCl played a dual role in simultaneously achieving

477   energy and nutrient recovery. In addition to the enhanced fuel quality and carbon utilization,

478   HCl extracted the P from the feedstocks into soluble PO_4^{3-}. The recirculated Ca- and P-rich PW

479   then recovered P in the form of Ca-associated P deposits (*e.g.,* hydroxyapatite) on the

480   hydrochar as a slow-release fertilizer. There are commercially available technologies for P and

481   N recovery, such as "Quick Wash" by liquid lime and organic poly-electrolyte (~90% P

482   recovery), "Cambi" by ferric chloride (up to 70% P recovery), and "PHOSPAQ^{TM}" by

483   magnesium oxide (70−95% of P recovery) (Aragón-Briceño et al., 2021). In comparison, this

484   study was able to achieve > 93% P recovery from the PW by utilizing the inherent Ca from the

485   digestate without applying additional chemicals for precipitation or separation. The market

486   price of hydroxyapatite (a representative compound for Ca-P deposit) is high as ~10,000 USD

487   ton^{-1}, which is 80-fold the price of P rock and 18-fold the price of struvite (Zhang et al., 2022).

488   This study provided a novel strategy to valorize the food waste digestate into a multifunctional

489   hydrochar as a high-quality solid fuel (P_R1/C_R1) and as an N- and P-rich slow-release

490   fertilizer (hydrochar from R2 to R6), while minimizing the wastewater discharge at the same

491   time.

492   To realize the large-scale valorization of FWD and YW *via* catalytic-HTC process with

493   PW recirculation, it is necessary to address several challenges in future investigations. (1) Due

to seasonal variation, regional difference, and upstream AD conditions, the properties of FWD and YW should be carefully characterized before production with optimized conditions. Using computational simulations with data mining such as machine learning could help to reveal the variation of physicochemical properties of feedstocks and suggest the corresponding HTC conditions to achieve robust production (He et al., 2022). (2) Recirculating the freshly produced PW with an elevated temperature can save energy consumption for the heating process and minimize wastewater discharge, which should be properly appraised in field-scale studies with a comprehensive life cycle assessment (LCA) and techno-economic analysis (TEA). (3) The potential of downstream methane production and energy balance from the C- and N-rich PW deserve further evaluation (e.g., biochemical methane potential (BMP) tests). (4) The agronomic/combustion performance and environmental safety of hydrochar as a slow-release fertilizer or solid fuel should be validated by pilot-scale site trials.

4   Conclusions

Calcium accumulation and acid catalyst during the PW recirculation facilitated the solid-liquid transformation of hydrochar and nutrients. HCl played a dual role in (i) catalyzing the HTC process to obtain the hydrochar with a high energy potential (HHV = 27.9 MJ kg^{-1}; FR = 0.87) and stable combustion behavior, and (ii) augmenting the extraction of P from the feedstock into soluble PO_4^{3-} (3150 mg L^{-1}) for nutrient recovery. By recirculating the PW, the inherent Ca was accumulated in the catalytic HTC system, which not only recovered the dissolved PO_4^{3-} as Ca-P deposits but also enhanced the hydrochar yield by 18−64%.

26

514 **Supplementary materials**

515 E-supplementary data for this work can be found in e-version of this paper online.

516

517 **Acknowledgment**

520 **Table 1.** Effects of HTC PW recirculation on energy properties of hydrochar

Feedstock	Conditions	HHV*	Key findings
Sweet potato waste [a] HHV* = 18.7 MJ kg^{-1}	220 °C; 1 h; RT* = 4	An increase of 0.7 MJ kg^{-1}	• PW recirculation significantly increased hydrochar yield • High thermal stability components were formed during the circulation step.
Brewer spent grains [b] HHV = 22.3 MJ kg^{-1}	200, 220 °C; 2−4 h; RT = 2	An increase of 0.2−0.6 MJ kg^{-1}	• Accumulation of organic acids catalyzed the HTC reactions • PW recirculation promoted the secondary char reactions
Food and yard waste [c] HHV = 14.0 MJ kg^{-1}	220 °C; 1 h; RT = 5	An increase of 1.4 MJ kg^{-1}	• High organic and ionic species in PW facilitated the carbonization process • The resultant PW has high anaerobic degradability
Sewage sludge [d] HHV = 10.3 MJ kg^{-1}	200 °C; RT = 4	An increase of 1.6 MJ kg^{-1}	• The main reactions of PW recirculation were dehydration and decarboxylation. • pH increased due to the accumulation of NH_4^+
	230 °C; RT = 4	A decrease of 0.5 MJ kg^{-1}	
	260 °C; RT = 4	An increase of 0.4 MJ kg^{-1}	
Poultry litter [e] HHV = 14.2 MJ kg^{-1}	200, 250 °C; 1 h RT = 5	An increase of 2.9−5.1 MJ kg^{-1}	• TOC and TN increased from Cycle 1 to 3 and remained steady from Cycle 4 to 5. • PW recirculation enhanced nutrient solubilization without changing hydrochar energy properties
Microalgae *Chlorella* [f] HHV =	300 °C; 0.5 h; RT = 4	An increase of 2.1 MJ kg^{-1}	• The PW exhibited high biodegradability for fungal-microalgal cultivation • Lignin/carboxylic-rich alicyclic molecules in PW have low biodegradability

521 *HHV = Higher heating value; RT = Recirculation times.

522 [a] (Chen et al., 2018); [b] (Arauzo et al., 2020); [c] (Sharma et al., 2022); [d] (Xu et al., 2020); [e] (Mau et al., 2019); [f] (Chen et al., 2022).

523 **Table 2.** Proximate, ultimate, and composition analysis of feedstocks

Feedstock	Proximate analysis (wt.% dry basis)			Ultimate analysis (wt.% dry basis)					Composition (wt.% dry basis)		
	VM	FC	Ash	C	H	N	S	O	Hemicellulose	Cellulose	Lignin
Food Waste Digestate (FWD)	65.7	3.8	30.5	32.9	3.0	4.0	0.2	29.4	9.4	7.2	12.2
Yard Waste (YW)	74.1	13.3	12.6	39.4	5.3	1.0	0.5	41.3	6.1	21.0	30.2

524

525 **Table 3.** Energy properties and combustion characteristic parameters of hydrochar with HTC process water recirculation

Hydrochar samples	Energy properties					Combustion properties						
	Solid yield (/)	HHV (MJ kg^{-1})	Energy recovery (/)	Fuel ratio (/)	C retention in hydrochar (/)	DTG_m (% min^{-1})	DTG_{mean} (% min^{-1})	T_m (°C)	T_i (°C)	T_b (°C)	CCI (10^{-7} %^{2} min^{-2} °C^{-3})	R_w (/)
P_R1	0.33	27.93	0.59	0.87	0.56	9.9	2.1	454	202	547	11.0	10.2
P_R2	0.43	23.81	0.68	0.52	0.49	7.2	1.7	407	236	508	4.2	6.4
P_R3	0.41	24.22	0.66	0.41	0.48	7.0	1.8	492	215	539	4.9	5.6
P_R4	0.41	28.34	0.77	0.52	0.49	7.8	1.9	492	211	559	5.9	6.5
P_R5	0.39	24.09	0.63	0.50	0.41	6.7	1.8	492	202	565	5.1	5.8
P_R6	0.39	24.93	0.66	0.39	0.38	7.8	1.8	492	191	551	6.9	7.1
C_R1	0.32	27.90	0.59	0.87	0.55	9.9	2.1	454	202	547	11.0	10.2
C_R2	0.54	21.83	0.79	0.71	0.62	6.9	1.7	413	230	547	4.1	6.2
C_R3	0.49	23.75	0.78	0.64	0.59	7.6	1.8	428	215	541	5.4	7.1
C_R4	0.42	24.93	0.71	0.63	0.50	7.8	1.9	489	239	541	4.7	5.7
C_R5	0.43	24.73	0.71	0.60	0.48	7.4	1.9	492	236	595	4.2	5.5
C_R6	0.41	23.87	0.65	0.55	0.44	7.5	1.9	492	228	567	4.8	5.7

526

527 **Table 4.** Assumptions and unit prices for cost-benefit calculation

Assumption
1. Electricity input for heating process is the same for each process with same temperature, holding time, solution volume, and solid loading rate
2. Water retained in hydrochar = 10% (removed by drying process)
3. Same cost/energy consumption for liquid and solid operation process (e.g., pumping, solid-liquid separation, and product dewatering/drying)
4. Hydrochar is the only product for solid fuel application by using energy recovery as indicator

Item	Price	Unit
Hydrochloric acid (37%)	0.94[a]	USD/L
Water	5.90E-05[b]	USD/L
Hydrochar	30[c]	USD/GJ HHV
Industrial wastewater treatment	1.25E-03[d]	USD/L

528 [a] (Jafari et al., 2021); [b] (HKWSD, 2021); [c] (IEA, 2020); [d] (USDOE, 2017).

529   1. Aragón-Briceño, C.I., Pozarlik, A.K., Bramer, E.A., Niedzwiecki, L., Pawlak-Kruczek,

530   H., Brem, G., 2021. Hydrothermal carbonization of wet biomass from nitrogen and

531   phosphorus approach: A review. *Renew Energy,* **171**, 401-415.

532   2. Arauzo, P.J., Olszewski, M.P., Wang, X., Pfersich, J., Sebastian, V., Manyà, J., Hedin, N.,

533   Kruse, A., 2020. Assessment of the effects of process water recirculation on the surface

534   chemistry and morphology of hydrochar. *Renew Energy*, **155**, 1173-1180.

535   3. Barta, K., Ford, P.C., 2014. Catalytic Conversion of Nonfood Woody Biomass Solids to

536   Organic Liquids. *Acc Chem Res*, **47**, 1503-1512.

537   4. Cao, Y., He, M., Dutta, S., Luo, G., Zhang, S., Tsang, D.C.W., 2021. Hydrothermal

538   carbonization and liquefaction for sustainable production of hydrochar and aromatics.

539   *Renew Sust Energ Rev*, **152**, 111722.

540   5. Carstea, E.M., Bridgeman, J., Baker, A., Reynolds, D.M., 2016. Fluorescence

541   spectroscopy for wastewater monitoring: A review. *Water Res*, **95**, 205-219.

542   6. Chen, J., Zhang, J., Pan, W., An, G., Deng, Y., Li, Y., Hu, Y., Xiao, Y., Liu, T., Leng, S.,

543   Chen, J., Li, J., Peng, H., Leng, L., Zhou, W., 2022. A novel strategy to simultaneously

544   enhance bio-oil yield and nutrient recovery in sequential hydrothermal liquefaction of high

545   protein microalgae. *Energy Convers Manag*, **255**, 1.

546   7. Chen, X., Ma, X., Peng, X., Lin, Y., Wang, J., Zheng, C., 2018. Effects of aqueous phase

547   recirculation in hydrothermal carbonization of sweet potato waste. *Bioresour Technol*,

548   **267**, 167-174.

549   8. Coble, P.G., Spencer, R.G.M., Baker, A., Reynolds, D.M., 2014. Aquatic Organic Matter

550   Fluorescence. in: *Aquatic Organic Matter Fluorescence*, (Eds.) A. Baker, D.M. Reynolds,

551   J. Lead, P.G. Coble, R.G.M. Spencer, Cambridge University Press. 75-122.

552   9.   Dutta, S., He, M., Xiong, X., Tsang, D.C.W., 2021. Sustainable management and recycling

553   of food waste anaerobic digestate: A review. *Bioresour Technol*, **341**, 125915.

554   10. Feng, D., Zhao, Y., Zhang, Y., Xu, H., Zhang, L., Sun, S., 2018. Catalytic mechanism of

555   ion-exchanging alkali and alkaline earth metallic species on biochar reactivity during

556   CO2/H2O gasification. *Fuel*, **212**, 523-532.

557   11. Gupta, J., Papadikis, K., Konysheva, E.Y., Lin, Y., Kozhevnikov, I.V., Li, J., 2021. CaO

558   catalyst for multi-route conversion of oakwood biomass to value-added chemicals and fuel

559   precursors in fast pyrolysis. *Appl Catal*, **285**, 119858.

560   12. Hao, X., Wang, X., Liu, R., Li, S., van Loosdrecht, M.C.M., Jiang, H., 2019.

561   Environmental impacts of resource recovery from wastewater treatment plants. *Water Res*,

562   **160**, 268-277.

563   *13.* He, M., Xu, Z., Hou, D., Gao, B., Cao, X., Ok, Y.S., Rinklebe, J., Bolan, N.S., Tsang,

564   D.C.W., 2022. Waste-derived biochar for water pollution control and sustainable

565   development. *Nat Rev Earth Environ,* **3**, 444-460.

566   14. He, M., Xu, Z., Sun, Y., Chan, P.S., Lui, I., Tsang, D.C.W., 2021a. Critical impacts of

567   pyrolysis conditions and activation methods on application-oriented production of wood

568   waste-derived biochar. *Bioresour Technol*, **341**, 125811.

569   15. He, M., Zhu, X., Dutta, S., Kumar Khanal, S., Teong Lee, K., Masek, O., Tsang, D.C.W.,

570   2021b. Catalytic co-hydrothermal carbonization of food waste digestate and yard waste

571   for energy application and nutrient recovery. *Bioresour Technol*, **344**, 126395.

572   16. HKWSD. 2021 Water and Sewage Tariff: Non-domestic Supplies.

573   17. Huang, W., Huang, W., Li, H., Lei, Z., Zhang, Z., Tay, J.H., Lee, D.-J., 2015. Species and

574   distribution of inorganic and organic phosphorus in enhanced phosphorus removal aerobic

575   granular sludge. *Bioresour Technol*, **193**, 549-552.

576   18. IEA. 2020. Renewables 2020-Analysis and forecast to 2025. International Energy

577   Association.

578   19. Jafari, M., Vanoppen, M., van Agtmaal, J.M.C., Cornelissen, E.R., Vrouwenvelder, J.S.,

579   Verliefde, A., van Loosdrecht, M.C.M., Picioreanu, C., 2021. Cost of fouling in full-scale

580   reverse osmosis and nanofiltration installations in the Netherlands. *Desalination*, **500**.

581   20. Kok, M.V., Gundogar, A.S., 2013. DSC study on combustion and pyrolysis behaviors of

582   Turkish crude oils. *Fuel Process Technol,* **116**, 110-115.

583   21. Lehmann, J., Cowie, A., Masiello, C.A., Kammann, C., Woolf, D., Amonette, J.E.,

584   Cayuela, M.L., Camps-Arbestain, M., Whitman, T., 2021. Biochar in climate change

585   mitigation. *Nat Geosci*, **14**, 883-892.

586   22. Leng, L., Yang, L., Leng, S., Zhang, W., Zhou, Y., Peng, H., Li, H., Hu, Y., Jiang, S., Li,

587   H., 2021. A review on nitrogen transformation in hydrochar during hydrothermal

588   carbonization of biomass containing nitrogen. *Sci Total Environ*, **756**, 143679.

589   23. Leng, S., Leng, L., Chen, L., Chen, J., Chen, J., Zhou, W., 2020. The effect of aqueous

590   phase recirculation on hydrothermal liquefaction/carbonization of biomass: A review.

591   *Bioresour Technol*, **318**, 124081.

592   24. Li, M., Zhang, A., Wu, H., Liu, H., Lv, J., 2017. Predicting potential release of dissolved

593   organic matter from biochars derived from agricultural residues using fluorescence and

594   ultraviolet absorbance. *J Hazard Mater*, **334**, 86-92.

595   25. Liu, H., Basar, I.A., Nzihou, A., Eskicioglu, C., 2021a. Hydrochar derived from municipal

596   sludge through hydrothermal processing: A critical review on its formation,

597   characterization, and valorization. *Water Res*, **199**, 117186.

598   26. Liu, T., Gao, X., Mofrad, A.Z., Kudo, S., Asano, S., Hayashi, J.I., 2021b. Leaching char

599   with acidic aqueous phase from biomass pyrolysis: Removal of alkali and alkaline-earth

600   metallic species and uptakes of water-soluble organics. *Energy Fuels*, **35**, 12237-12251.

601   27. Lucian, M., Volpe, M., Gao, L., Piro, G., Goldfarb, J.L., Fiori, L., 2018. Impact of

602   hydrothermal carbonization conditions on the formation of hydrochars and secondary

603   chars from the organic fraction of municipal solid waste. *Fuel*, **233**, 257-268.

604   28. Mau, V., Neumann, J., Wehrli, B., Gross, A., 2019. Nutrient behavior in hydrothermal

605   carbonization aqueous phase following recirculation and reuse. *Environ Sci Technol*, **53**,

606   10426-10434.

607   29. McKinsey&Company. 2021. Managing water and climate risk with renewable energy.

608   30. Monlau, F., Sambusiti, C., Ficara, E., Aboulkas, A., Barakat, A., Carrère, H., 2015. New

609   opportunities for agricultural digestate valorization: Current situation and perspectives.

610   *Energy Environ Sci*, **8**, 26-2621.

611   31. Nan, H., Yin, J., Yang, F., Luo, Y., Zhao, L., Cao, X., 2021. Pyrolysis temperature-

612   dependent carbon retention and stability of biochar with participation of calcium:

613   Implications to carbon sequestration. *Environ Pollut*, **287**, 117566.

614   32. Nicolae, S.A., Au, H., Modugno, P., Luo, H., Szego, A.E., Qiao, M., Li, L., Yin, W.,

615   Heeres, H.J., Berge, N., Titirici, M.M., 2020. Recent advances in hydrothermal

616   carbonisation: From tailored carbon materials and biochemicals to applications and

617   bioenergy. *Green Chem*, **22**, 4747-4800.

618   33. Ruban, V., López-Sánchez, J.F., Pardo, P., Rauret, G., Muntau, H., Quevauviller, P., 1999.

619   Selection and evaluation of sequential extraction procedures for the determination of

620   phosphorus forms in lake sediment. *J Environ Monit*, **1**, 51-56.

621   34. Sans, J., Sanz, V., Turon, P., Alemán, C., 2021. Enhanced CO2 conversion into ethanol by

622   permanently polarized hydroxyapatite through C−C coupling. *ChemCatChem*, **13**, 5025-

623   5033.

624   35. Sharma, H.B., Panigrahi, S., Vanapalli, K.R., Cheela, V.R.S., Venna, S., Dubey, B., 2022.

625   Study on the process wastewater reuse and valorisation during hydrothermal co-

626   carbonization of food and yard waste. *Sci Total Environ*, **806**, 150748.

627   36. Shi, Y., Chen, Z., Cao, Y., Fan, J., Clark, J.H., Luo, G., Zhang, S., 2021. Migration and

628   transformation mechanism of phosphorus in waste activated sludge during anaerobic

629   fermentation and hydrothermal conversion. *J Hazard Mater*, **403**, 123649.

630   37. Shi, Y., Luo, G., Rao, Y., Chen, H., Zhang, S., 2019. Hydrothermal conversion of

631   dewatered sewage sludge: Focusing on the transformation mechanism and recovery of

632   phosphorus. *Chemosphere*, **228**, 619-628.

633   38. Song, C., Shan, S., Yang, C., Zhang, C., Zhou, X., Ma, Q., Yrjälä, K., Zheng, H., Cao, Y.,

634   2020. The comparison of dissolved organic matter in hydrochars and biochars from pig

635   manure. *Sci Total Environ*, **720**, 137423.

636   39. Stedmon, C.A., Bro, R., 2008. Characterizing dissolved organic matter fluorescence with

637   parallel factor analysis: a tutorial. *Limnol Oceanogr Methods*, **6**, 572-579.

638   40. USDOE. 2017. Water and wastewater annual price escalation rates for selected cities

639   across the United States. U.S. Department of Energy. Office of Energy Efficiency &

640   Renewable Energy.

641   41. Usman, M., Chen, H., Chen, K., Ren, S., Clark, J.H., Fan, J., Luo, G., Zhang, S., 2019.

642   Characterization and utilization of aqueous products from hydrothermal conversion of

643   biomass for bio-oil and hydro-char production: A review. *Green Chem*, **21**, 1553-1572.

644   42. Wang, F., Wang, J., Gu, C., Han, Y., Zan, S., Wu, S., 2019. Effects of process water

645   recirculation on solid and liquid products from hydrothermal carbonization of Laminaria.

646   *Bioresour Technol*, **292**, 121996.

647   43. Xiao, K., Shen, Y., Liang, S., Tan, J., Wang, X., Liang, P., Huang, X., 2018. Characteristic

648   regions of the fluorescence excitation–emission matrix (EEM) to identify

649   hydrophobic/hydrophilic contents of organic matter in membrane bioreactors. *Environ Sci*

650   *Technol*, **52**, 11251-11258.

651   44. Xu, Z.-X., Song, H., Li, P.-J., He, Z.-X., Wang, Q., Wang, K., Duan, P.-G., 2020.

652   Hydrothermal carbonization of sewage sludge: Effect of aqueous phase recycling. *Chem*

653   *Eng J*, **387**, 123410.

654   45. Yang, T., Du, C., Li, B., Liu, Z., Kai, X., 2022. Influence of alkali and alkaline earth metals

655 on the hydrothermal liquefaction of lignocellulosic model compounds. *Renew Energy*,

656 **188**, 1038-1048.

657 46. Yuan, S., Tan, Z., Huang, Q., 2018. Migration and transformation mechanism of nitrogen

658 in the biomass–biochar–plant transport process. *Renew Sust Energ Rev*, **85**, 1-13.

659 47. Zhang, C., Guisasola, A., Baeza, J.A., 2022. A review on the integration of mainstream P-

660 recovery strategies with enhanced biological phosphorus removal. *Water Res*, **212**,

661 118102.

662 48. Zhang, H., Xue, G., Chen, H., Li, X., 2019. Hydrothermal synthesizing sludge-based

663 magnetite catalyst from ferric sludge and biosolids: Formation mechanism and catalytic

664 performance. *Sci Total Environ*, **697**, 133986.

665 49. Zheng, X., Ye, Y., Jiang, Z., Ying, Z., Ji, S., Chen, W., Wang, B., Dou, B., 2020. Enhanced

666 transformation of phosphorus (P) in sewage sludge to hydroxyapatite via hydrothermal

667 carbonization and calcium-based additive. *Sci Total Environ*, **738**, 139786.

668